Volume 15
Number 4
28 January 2023
Pages 1443-1964

Nanoscale

rsc.li/nanoscale

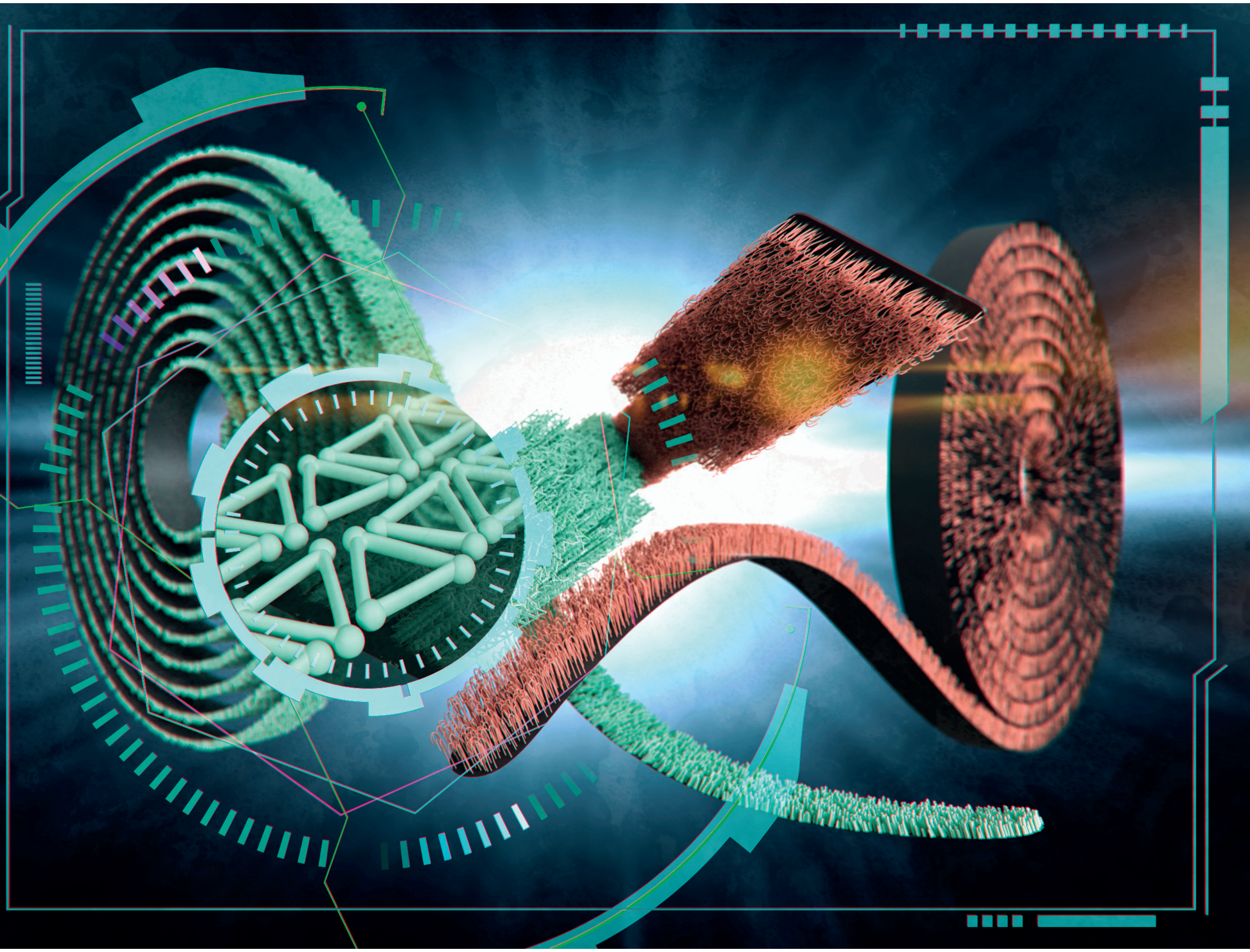

ISSN 2040-3372

ROYAL SOCIETY
OF **CHEMISTRY**

PAPER
Václav Houska, Irena G. Stará, Bohuslav Rezek,
Ivo Starý *et al.*
Helicene-based π-conjugated macrocycles: their synthesis, properties, chirality and self-assembly into molecular stripes on a graphite surface

NCNST

Nanoscale

ROYAL SOCIETY OF CHEMISTRY

PAPER

View Article Online
View Journal | View Issue

Check for updates

Cite this: *Nanoscale*, 2023, **15**, 1542

Helicene-based π-conjugated macrocycles: their synthesis, properties, chirality and self-assembly into molecular stripes on a graphite surface†

Václav Houska,*[a,b] Egor Ukraintsev,[c,d] Jaroslav Vacek,[b] Jiří Rybáček,[b] Lucie Bednárová,[b] Radek Pohl,[b] Irena G. Stará, *[b] Bohuslav Rezek *[d] and Ivo Starý *[b]

Received 29th July 2022,
Accepted 21st October 2022

DOI: 10.1039/d2nr04209f

rsc.li/nanoscale

Fully aromatic helicenes are attractive building blocks for the construction of inherently chiral π-conjugated macrocyclic nanocarbons. These hitherto rare molecular architectures are envisaged to exhibit remarkable (chir)optical properties, self-assembly, charge/spin transport, induced ring current or a fascinating Möbius topology. Here the synthesis of helically chiral macrocycles that combine angular dibenzo[5]helicene units as corners and linear *trans*-stilbene-4,4′-diyl linkers as edges is reported. By subjecting a racemic or enantiopure divinyl derivative of dibenzo[5]helicene to olefin metathesis, which was catalysed by a 2nd generation Piers catalyst under kinetic control, a π-conjugated helicene cyclic trimer (33%) and a tetramer (22%) were obtained, which were separated by GPC. Combining racemic/asymmetric synthesis with the resolution of enantiomers/diastereomers by SFC/HPLC on a chiral column, both homochiral (+)-(*M*,*M*,*M*)/(−)-(*P*,*P*,*P*) and heterochiral (+)-(*M*,*M*,*P*)/(−)-(*M*,*P*,*P*) stereoisomers of the helicene cyclic trimer could be obtained in an enantio- and diastereomerically enriched form. The complete energy profile of their interconversion was compiled on the basis of kinetic measurements and numerical solution of the proposed kinetic model. In equilibrium, the heterochiral diastereomer predominates over the homochiral one (*ca.* 75 : 25 at 76 °C). π-Conjugation along a large, twisted circuit in the helicene cyclic trimer is rather disrupted, stabilising this formally antiaromatic molecule. Using an optimised PeakForce mode of ambient AFM, the self-assembly of otherwise highly mobile stereoisomers of the helicene cyclic trimer on the HOPG surface could be studied. Irrespective of the stereochemistry, strong preferences for the edge-to-edge interaction of these macrocycles were found to form very long parallel 1D molecular stripes in ordered 2D nanocrystals, a result also supported by molecular dynamics simulations. Six trityl groups, initially introduced to the macrocycle to enhance solubility, serve as a key "molecular Velcro" system in the self-assembly of macrocycles to maximise their mutual van der Waals interactions.

Introduction

In the realm of chiral nanocarbons in a broader sense, helicene-derived macrocycles are not common but attractive synthetic targets. Their design and preparation could now benefit from a number of accessible helicene building blocks,[1] variability of interconnecting units and different ways of cyclooligomerisation of the corresponding bifunctional (helicene) monomers, *vide infra*. Helicene-derived macrocycles were pioneered by Thulin and Wennerström[2] in 1976 who prepared the racemic figure-of-eight propellicene composed of two homochiral [5]helicene units. With a time lag of two decades, in 1996, Yamaguchi and co-workers[3,4] and, in 1998, Fox and co-workers[5] prepared enantiopure cycloamides containing **1–4** homochiral conformationally locked (*M*)- or (*P*)-[4]helicene units and enantiopure helical acetylene-bridged cyclophane

---

[a] *Department of Physical and Macromolecular Chemistry, Faculty of Science, Charles University in Prague, Hlavova 8, 128 43 Prague 2, Czech Republic. E-mail: houska@uochb.cas.cz*
[b] *Institute of Organic Chemistry and Biochemistry, Czech Academy of Sciences, Flemingovo nám. 2, 166 10 Prague 6, Czech Republic. E-mail: stara@uochb.cas.cz, stary@uochb.cas.cz*
[c] *Institute of Physics, Czech Academy of Sciences, Cukrovarnická 10, 162 00 Prague 6, Czech Republic*
[d] *Department of Physics, Faculty of Electrical Engineering, CTU in Prague, Technická 2, 166 27 Prague 6, Czech Republic*

† Electronic supplementary information (ESI) available: Experimental procedures and characterisation data for **1b**, **2a**, **2b**, **3**, and **4**, chromatographic resolution of stereoisomers of **2b** and **3**, kinetic data of interconversion of stereoisomers of **3**, estimation of the enantiomerisation barrier of **1a** and **2b**, ECD spectra and absolute configuration assignment of **1a**, **2b** and **3**, AFM measurements of **3** and **4**, DFT calculation and MD simulation data and copies of NMR spectra. See DOI: https://doi.org/10.1039/d2nr04209f

built from two homochiral (*P*)-[6]helicene units, respectively. Later, in 2011, Isobe and co-workers[6] published the three-step synthesis of the configurationally unstable "Penrose stairs" dimer by connecting two homochiral [4]helicene units. In 2017, Durola, Bock and co-workers[7,8] revised the synthesis of the racemic figure-of-eight propellicene comprising two homochiral ethoxycarbonylated [5]helicenes, *cf.* ref. 2. The same year, Hiroto, Shinokubo and co-workers[9] described the synthesis of an enantiopure figure-of-eight azahelicene dimer formed from two homochiral π-extended (*M*)- or (*P*)-aza[5]helicene blocks. Most recently, in 2020, Tilley and co-workers[10] presented a configurationally labile figure-of-eight nanocarbon comprising two ethynylene-bridged homochiral expanded anthrahelicene subunits.

Although only three, spectacular examples of π-conjugated/cross-conjugated helicene cyclotrimers have been reported in the literature (Fig. 1, **A–C**). In 2003, Yamaguchi and co-workers[11] prepared an enantiopure cyclotrimer **A** made up of three ethynylene-bridged homochiral conformationally locked (*M*)-[4]helicene units, which were further dimerised *via* the azo group. In 2018 and 2020, Herges, Durola and co-workers[12] and Garcia-Garibay, Zhu, Moore and co-workers,[13] respectively, synthesised helicene cyclotrimers **B** and **C** with a fascinating Möbius topology. While in the first case the equally populated (and separated) diastereomeric cyclotrimers were composed of three either heterochiral or homochiral ethoxycarbonylated [5]helicenes directly connected through aryl–aryl bonds, in the second case the kinetically preferred diastereopure cyclotrimer was composed of three ethynylene-bridged heterochiral [5]helicenes.

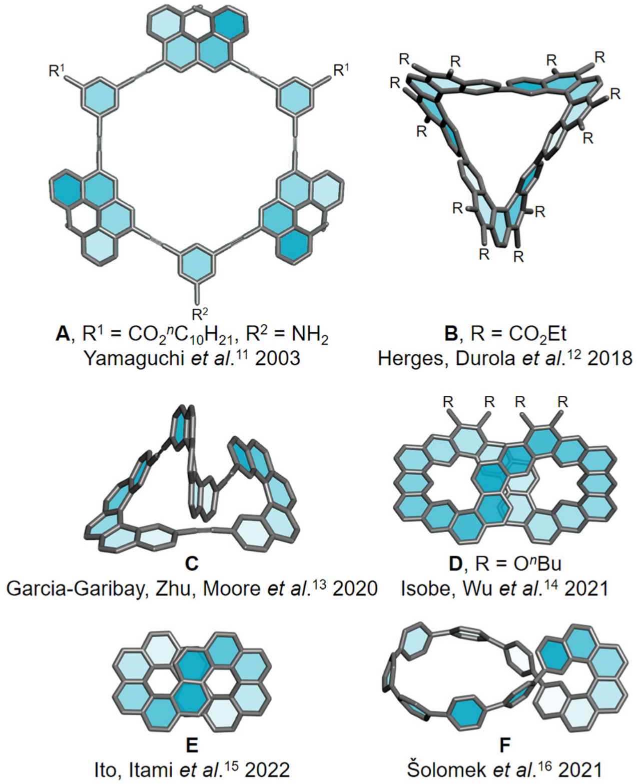

A, R^1 = CO$_2{}^n$C$_{10}$H$_{21}$, R^2 = NH$_2$
Yamaguchi *et al.*[11] 2003

B, R = CO$_2$Et
Herges, Durola *et al.*[12] 2018

C
Garcia-Garibay, Zhu, Moore *et al.*[13] 2020

D, R = O^{n}Bu
Isobe, Wu *et al.*[14] 2021

E
Ito, Itami *et al.*[15] 2022

F
Šolomek *et al.*[16] 2021

Fig. 1 So far described helicene-based macrocyclic trimers **A–C** and other recently reported helicene macrocycles **D–F** (hydrogen atoms have been omitted for clarity).

In the context of helicene-based macrocycles, but outside the above categories, three recent examples should be mentioned (Fig. 1, **D–F**). In 2021, Isobe, Wu and co-workers[14] reported a twisted carbon nanobelt **D** consisting of twenty annulated benzene rings. Almost simultaneously (in 2022), Ito, Itami and co-worker[15] prepared the racemic and enantiopure helically twisted [12]circulene **E**, a smaller variant of the above figure-of-eight nanocarbon. Last but not least, in 2021 Šolomek and co-workers[16] announced the successful preparation of a hybrid [7]cycloparaphenylene-[6]helicene Möbius-type figure-of-eight macrocycle **F**, both in racemic and enantiopure forms.

Despite the limited number of inherently chiral helicene-derived macrocycles prepared so far, their common chemical and physical properties have already been studied (crystal structure, enantiomerisation barrier, (chir)optical and electronic properties)[2–16] along with self-assembly at the air–water interface and the formation of chiral Langmuir–Blodgett films,[17] CPL emission,[9,15] self-aggregation,[6,11] aromaticity,[13,15,16] Möbius topology,[12,16] electrochemistry,[7,14] or their use in enantioselective catalysis.[4] However, to the best of our knowledge, their self-assembly on solid surfaces in 2D confined space, which calls for imaging by scanning probe microscopy (SPM) techniques, has so far only been addressed in our parallel study.[18,19]

Herein, the synthesis of helically chiral macrocycles from a racemic or enantiopure divinyl derivative of tritylated dibenzo[5]helicene *via* olefin metathesis is reported (Scheme 1). Irrespective of the stereochemistry, the preferentially formed six-fold tritylated macrocyclic trimer self-assembled into long 1D molecular stripes on the HOPG surface as detected by ambient AFM. The trityl groups apparently serve as effective "molecular Velcro".

Results and discussion

Synthesis of helicene macrocycles 3 and 4

In order to design large, π-conjugated and inherently chiral macrocycles, a combination of angular helicene units as corner structural elements and linear *trans*-stilbene-4,4′-diyl linkers as edges was chosen. Since it was not clear whether the helicene macrocycles such as **3** or **4** would favour homochiral or heterochiral helicene units, the racemic dibenzo[5]helicene building block **1a**[20] was selected (Scheme 1). It is synthetically accessible in a straightforward way[21] and is conformationally well-defined with moderate configurational stability at room temperature (barrier to enantiomerisation is 26.1 kcal mol^{-1}, see the ESI;† *cf.* a comprehensive study on the enantiomerisation barriers of [5]helicene derivatives, ref. 22). The nonplanar helicene units were also expected to ensure sufficient solubility of target macrocycle architectures, as such an effect was

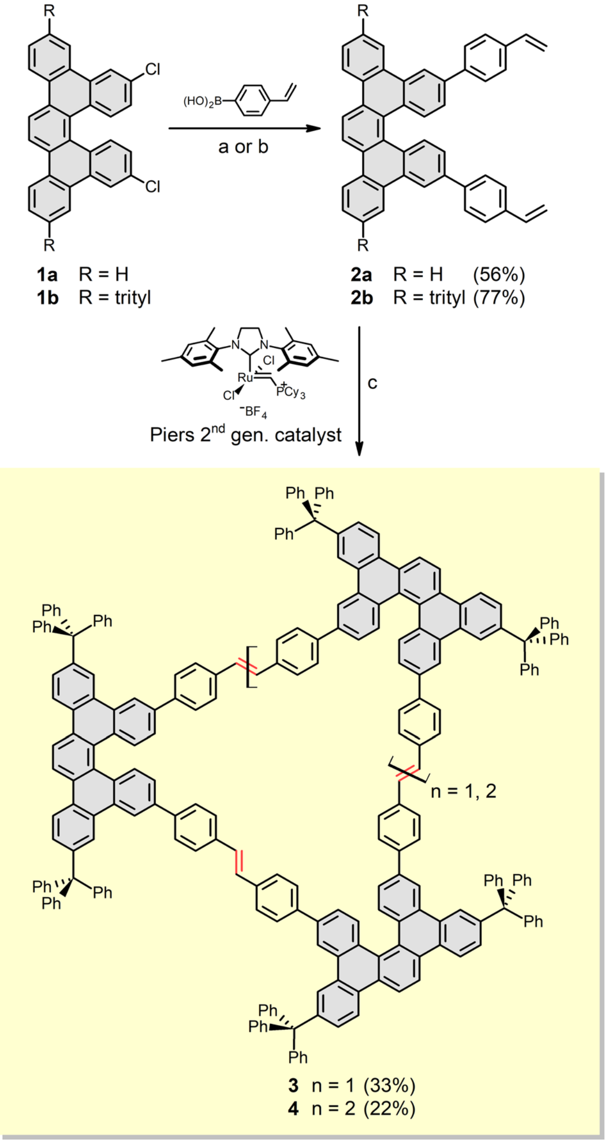

Scheme 1 Synthesis of dibenzo[5]helicene/*trans*-stilbene macrocycles **3** and **4** by olefin metathesis. Reaction conditions: (a) Pd(OAc)$_2$, XPhos, K$_3$PO$_4$, dioxane, 85 °C, 18 h (**1a** → **2a**); (b) XPhos Pd G2, K$_3$PO$_4$, THF, 100 °C, 3 h (**1b** → **2b**); (c) Piers 2nd gen. catalyst, 1,2,4-trichlorobenzene, vacuum, 50 °C, overnight (**2b** → **3** + **4**).

observed with multiple helicenes.[23] As a macrocycle-forming reaction, robust olefin metathesis allowing the construction of a π-conjugated system under kinetic/thermodynamic control was chosen. It is worth noting that olefin metathesis has not yet been used to form inherently chiral π-conjugated macrocycles derived from helicenes.

The starting dichlorodibenzo[5]helicene **1a** was first arylated to give the key divinyl derivative **2a**. Olefin metathesis was attempted using a second-generation Grubbs catalyst, but an inseparable mixture of completely insoluble oligomers was formed. The solubility of metathesis products was only marginally increased by equipping the starting divinyl derivative **2a** with longer alkyl or oligo(ethylene glycol) side chains, commonly used as solubilising groups. Therefore, bulky trityl groups[24] were introduced into the dibenzo[5]helicene building block **2b** to minimise π–π stacking between the large π-electron systems formed in the reaction.

Indeed, metathesis of the trityl-decorated divinyl derivative **2b** catalysed by a more reactive second-generation Piers catalyst[25] and performed in 1,2,4-trichlorobenzene (TCB) under vacuum led to the virtually complete conversion of the starting material and the formation of (cyclo)oligomeric products according to analytical gel permeation chromatography (GPC). After optimisation, the highest yields of macrocycles **3** and **4** were obtained when the reaction started at high dilution and then the mixture was gradually concentrated overnight by slow evaporation of TCB at 50 °C. The MALDI mass spectrum of the crude reaction mixture showed a significant peak at *m*/*z* 3116 with an extensive fragmentation pattern that corresponded to the cyclic trimer **3**, while the peak at *m*/*z* 4155 belonged to the cyclic tetramer **4** (Fig. 2). Peaks corresponding to the ions of acyclic counterparts were practically absent, indicating that the formation of cyclic oligomers was favoured. Repeated preparative GPC of a product mixture afforded the cyclic trimer **3** (33% yield) and cyclic tetramer **4** (22% yield) as the major products.

In order to distinguish whether the cyclic trimer **3** and tetramer **4** were formed under kinetic or thermodynamic control, the less abundant macrocycle **4** was subjected to the original

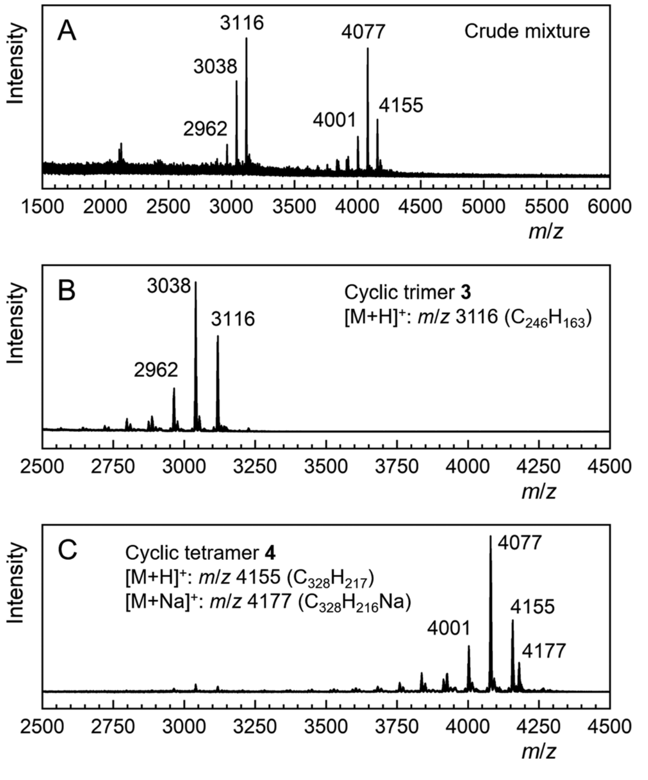

Fig. 2 MALDI mass spectra of the crude mixture of the olefin metathesis reaction of **2b** (A) and the cyclic trimer **3** (B) and tetramer **4** (C) isolated by GPC. Fragmentation of the trityl groups by multiple loss of the C$_6$H$_5$ group (M$^+$: *m*/*z* 77) is visible in the spectra (*m*/*z* peaks marked with monoisotopic mass).

metathesis reaction conditions (TCB, 50 °C). After 18 hours, only traces of the cyclic trimer **3** were detected by analytical GPC. However, when the temperature rose to 70 °C, GPC analysis and MALDI MS after further 14 hours showed a noticeable amount of **3**. In addition, a large amount of precipitate also formed which was attributed to the insoluble higher-order cyclic/linear oligomers (not detected by GPC but indicated by MALDI MS). Accordingly, these findings show a dominant role of the kinetic control in the metathesis of **2b** at 50 °C to deliver macrocycles **3** and **4**. At higher temperatures, the thermodynamic equilibration begins to operate, although it is at the same time disrupted by kinetically driven precipitation of higher-order oligomers.

Compared to the previous cases of helical macrocycle synthesis, it is worth noting that Zhang and co-workers demonstrated thermodynamic control in olefin metathesis to form an achiral *meta*-phenylenevinylene macrocycle following the principles of dynamic covalent chemistry,[26] but Moore and co-workers have recently described a remarkable kinetic selectivity in the synthesis of a chiral ethynylene[5]helicenylene Möbius-type cyclic trimer by alkyne metathesis.[13]

Stereochemistry of the helicene cyclic trimer 3

With respect to the chirality of the embedded dibenzo[5]helicene units, the cyclic trimer can exist in two diastereomeric forms, *i.e.*, homochiral (*M**,*M**,*M**)-**3** and heterochiral (*M**,*M**,*P**)-**3**, each as a pair of enantiomers (*M*,*M*,*M*)/(*P*,*P*,*P*) and (*M*,*M*,*P*)/(*M*,*P*,*P*), respectively (Fig. 3). By compromising the macrocycle size and the corresponding computational costs, the structure of the diastereomers (*M**,*M**,*M**)-**3** and (*M**,*M**,*P**)-**3** was optimised at the DFT level of theory (B3LYP/cc-pVDZ/GD3/PCM in chloroform) and the energy difference between them (ΔG) was calculated. Heterochiral (*M**,*M**,*P**)-**3** was found to be only about 0.1 kcal mol^{-1} more stable than homochiral (*M**,*M**,*M**)-**3** (experimental value is *ca.* 0.5 kcal mol^{-1}, *vide infra*).

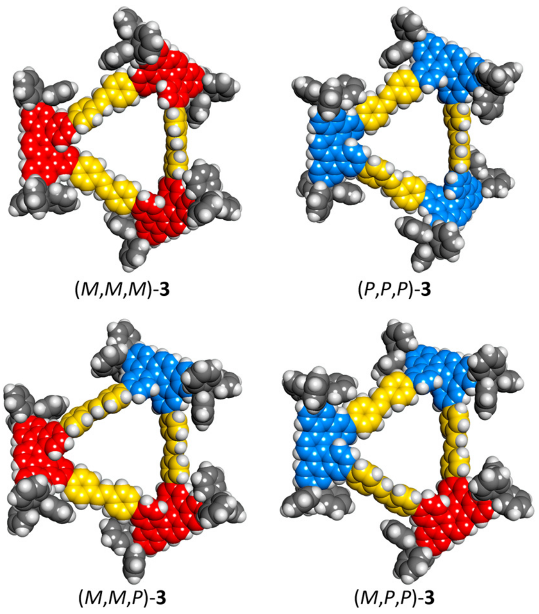

(*M*,*M*,*M*)-**3** (*P*,*P*,*P*)-**3**

(*M*,*M*,*P*)-**3** (*M*,*P*,*P*)-**3**

Fig. 3 Stereoisomers of the helicene cyclic trimer **3**; their structure was optimised by DFT (B3LYP/cc-pVDZ/GD3/PCM in chloroform) ((*M*)-dibenzo[5]helicene units in red, (*P*)-dibenzo[5]helicene units in blue, and *trans*-stilbene-4,4′-diyl linkers in yellow).

The ^{1}H NMR spectrum of the cyclic trimer showed the presence of both homochiral (*M**,*M**,*M**)-**3** and heterochiral (*M**,*M**,*P**)-**3** diastereomers whose signal sets were apparently very similar and overlapped. Using routine NMR techniques, it was possible to assign individual sets of signals to the distinguished diastereomers, but at this moment it could not be determined which is which. Integration of these signals revealed a 75 : 25 ratio at 76 °C between the two diastereomers (for a detailed discussion of the NMR signal assignment, see the ESI†).

The separation of diastereomers (*M**,*M**,*M**)-**3** and (*M**,*M**,*P**)-**3** by GPC was not possible. However, the analytical use of supercritical fluid chromatography (SFC) on a chiral column (Chiral ART Amylose-SA) led to the partial separation of the four stereoisomers into three peaks (Fig. 4A). The separation could be upscaled using semi-preparative HPLC on the same chiral stationary phase to obtain submilligramme amounts of materials.

To clarify the stereochemical issues, the macrocycle-forming reactions with individual enantiomers of the starting trityl-decorated divinyl derivative **2b** were performed. Thus, its racemate was resolved into (−)-(*M*)-**2b** (*ca.* 95% ee) and (+)-(*P*)-**2b** (*ca.* 95% ee) by HPLC on a semipreparative chiral column (Chiral ART Amylose-SA), the barrier to enantiomerisation of 26.1 kcal mol^{-1} ($t_{1/2}$ = 12.7 day at 22 °C) was experimentally determined and the helicity of the enantiomers was assigned by comparing the respective experimental *vs.* theoretical ECD spectra (for details, see the ESI†).

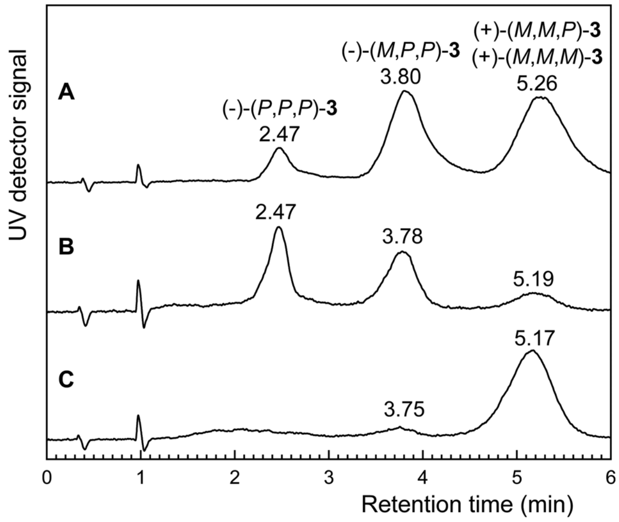

Fig. 4 Analytical separation of stereoisomers of the cyclic trimer **3** by SFC on a chiral column (Chiral ART Amylose-SA, carbon dioxide–chloroform–isopropanol, UV detection at 254 nm). The cyclic trimer **3** was synthesised from *rac*-**2b** (A) at 45 °C and from (+)-(*P*)-**2b** (B)/(−)-(*M*)-**2b** (C) at room temperature.

Highly enantioenriched (−)-(*M*)- and (+)-(*P*)-**2b** were subjected to metathesis macrocyclisation under similar conditions to racemic **2b** (*cf.* Scheme 1) but this time the reaction was run to completion under vacuum at room temperature (*ca.* 22 °C, two days) to minimise enantiomerisation of the dibenzo[5]helicene units. SFC analysis (Chiral ART Amylose-SA) showed that homochiral (−)-(*P*,*P*,*P*)-**3** or (+)-(*M*,*M*,*M*)-**3** prevailed in the fraction of stereoisomeric cyclic trimers (Fig. 4B and C). It should be noted that the stereochemical outcome of the macrocyclisation (degree of isomerisation) was influenced by the actual temperature and duration of the reaction/work-up and delay of the chiral SFC analysis. Accordingly, in a mixture of stereoisomers (Fig. 4A), the first peak at 2.47 min was the homochiral (−)-(*P*,*P*,*P*)-**3** and the peaks at 3.80 and 5.26 min were the resolved enantiomers of the heterochiral cyclic trimer **3**, the latter of which overlapped with the homochiral (+)-(*M*,*M*,*M*)-**3**. Based on further kinetic measurements and ECD spectra, *vide infra*, it was possible to assign the absolute configuration also to the individual enantiomers of the heterochiral cyclic trimer **3**: (−)-(*M*,*P*,*P*)-**3** formed the second peak at 3.80 min and (+)-(*M*,*M*,*P*)-**3** was a main component of the third peak at 5.26 min.

Interconversion of stereoisomers of the helicene cyclic trimer 3

To obtain a detailed picture of the interconversion of stereoisomers of the cyclic trimer **3**, attention was paid to the kinetics of the respective configurational changes. First, a 3 : 2 ratio between the extinction coefficients ε of heterochiral and homochiral diastereomers was elucidated from the SFC calibration curves to track properly the concentrations of individual stereoisomers in the SFC chromatograms (UV detector; for details, see the ESI†). Then, upon heating a highly enantioenriched (−)-(*P*,*P*,*P*)-**3** (>95% ee, >95% dr) to 76 °C, gradual equilibration between the stereoisomers was observed over time and the composition of the mixture was continuously monitored by SFC (Fig. 5A). A simple kinetic model was proposed to describe the interconversion of the stereoisomers of **3** (Fig. 5B). It was based on the assumption that the embedded dibenzo[5]helicene units invert their helicity independently (one after the other) through the C_s symmetric saddle-shaped transition state, which is typical of the enantiomerisation pathway of small helicenes.[27–29] The kinetic model (kinetics of three reversible consecutive reactions) was described by a system of rate equations (for details, see the ESI†), which were numerically solved and fitted to the experimental data. Based on these calculations, the proposed kinetic model turned out to be in very convincing agreement with the experimental data, giving the following values of the rate constants: $k_1 = 8 \times 10^{-4}\ \mathrm{s}^{-1}$, $k_{-1} = 4 \times 10^{-4}\ \mathrm{s}^{-1}$ and $k_2 = 6 \times 10^{-4}\ \mathrm{s}^{-1}$ (*cf.* Fig. 5B).

Then, using the Eyring–Polanyi equation, it was possible to calculate the respective free energy barriers and plot the energy profile of the whole interconversion of the stereoisomers of **3** (Fig. 6). Based on kinetic measurements, the free energy difference ΔG between the major heterochiral (+)-(*M*,*M*,*P*)- or (−)-(*M*,*P*,*P*)-**3** and the minor homochiral (+)-(*M*,*M*,*M*)- or (−)-(*P*,*P*,*P*)-**3** is 0.5 kcal mol^{-1}, which corresponds to their 67 : 33 ratio in equilibrium at 76 °C. It is in reasonable agreement with the value of 75 : 25 at the same temperature as inferred from the ^{1}H NMR spectrum, *vide supra*. The experimentally estimated enantiomerisation barrier between the heterochiral enantiomers (+)-(*M*,*M*,*P*)-**3** and (−)-(*M*,*P*,*P*)-**3** is 25.6 kcal mol^{-1} and the enantiomerisation barrier between the homochiral enantiomers (+)-(*M*,*M*,*M*)-**3** and (−)-(*P*,*P*,*P*)-**3** is 26.1 kcal mol^{-1}. These values are thus practically identical to the values of the enantiomerisation barrier measured for the monomer building blocks **1a** (26.1 kcal mol^{-1}) or **2b** (26.1 kcal mol^{-1}; for details, see the ESI†). This means that the dibenzo[5]helicene subunits tied up in the cyclic trimer **3** are not extra rigidised and also the rotational reorganisation of the trityl groups during the enantiomerisation process has no effect on its energy barrier. It is worth noting that all ground-state and transition-state stereoisomers are chiral, with the exception of TS (*M*,*saddle*,*P*)-**3**, which is the *meso* form, and thus achiral.

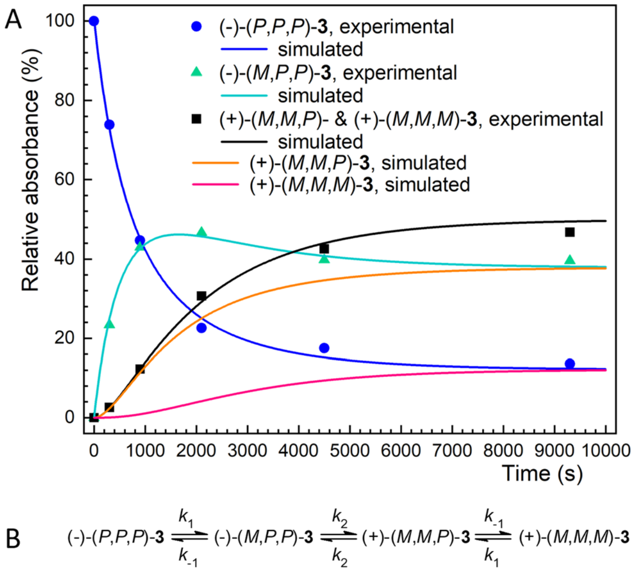

Fig. 5 Kinetics of the interconversion of the stereoisomers of **3** (at 76 °C in chloroform, in a closed vial): (A) comparison of experimental data and the proposed kinetic model (B) (relative absorbance is used instead of relative concentration; for details, see the ESI†).

The aforementioned inversion barriers for the stereoisomers of **3** were also calculated by computational methods (Fig. 6). Both homochiral and heterochiral diastereomers were first subjected to molecular dynamics simulations under vacuum (applying the ReaxFF force field)[30] to select the four most energetically favoured conformers for each diastereomer. The structures were optimised at the DFT (B3LYP/cc-pVDZ/GD3/PCM) level of theory in chloroform to calculate the respective free energies (for details, see the ESI†). The obtained results were fully consistent with the experimental data, further supporting the validity of the proposed kinetic model.

Stereochemistry of the helicene cyclic tetramer 4

The stereochemistry of the cyclic tetramer **4** is even more complex. It can exist in the form of two chiral (M^*,M^*,M^*,M^*)

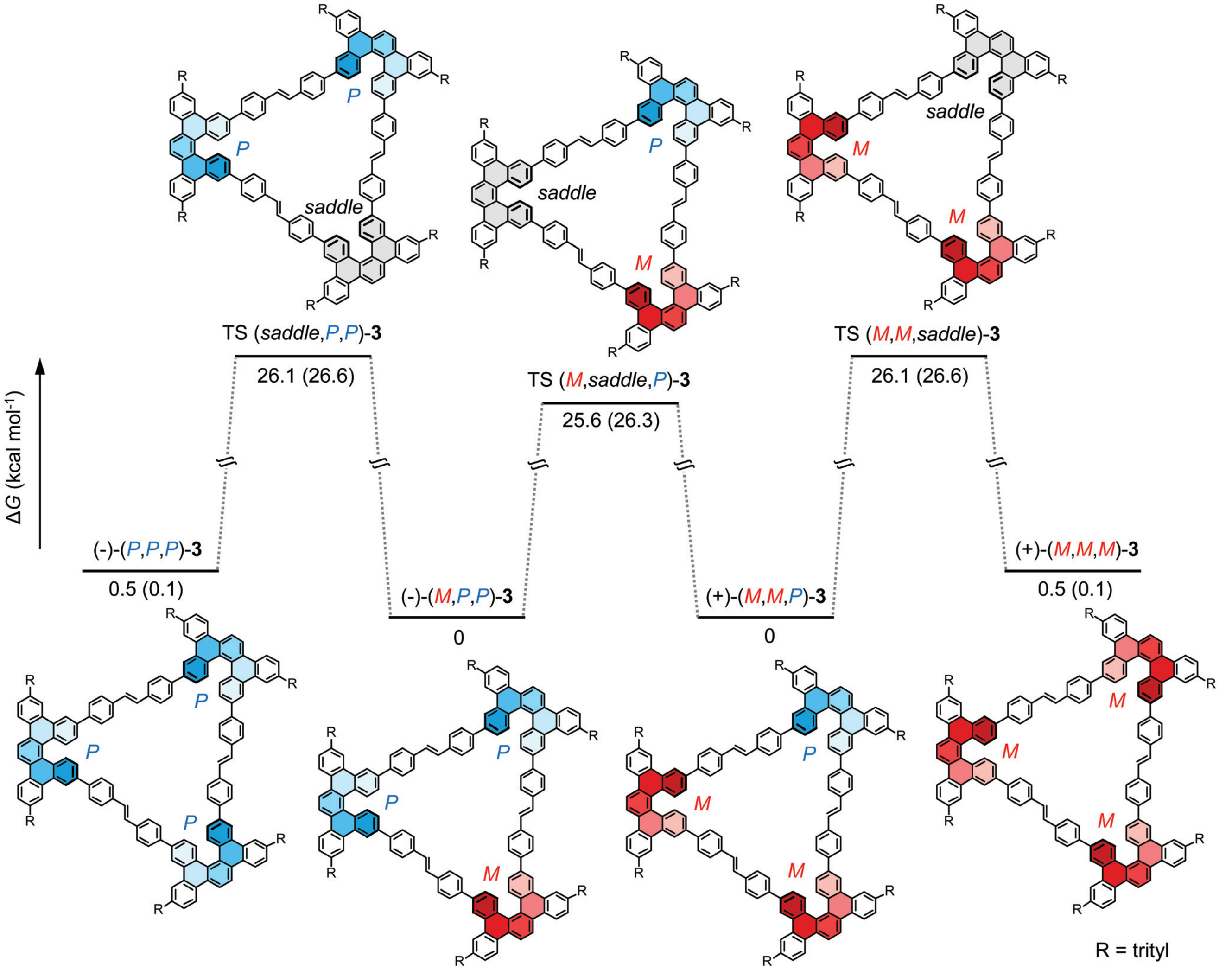

Fig. 6 Energy profile of the interconversion of the respective stereoisomers of **3** in chloroform based on experimental data (kinetic measurements), the proposed kinetic model and its numerical simulation. The free energies calculated by DFT (B3LYP/cc-pVDZ/GD3/PCM) in chloroform are given in parentheses.

and (*M**,*M**,*M**,*P**) diastereomers and two achiral (*M**,*M**,*P**,*P**) and (*M**,*P**,*M**,*P**) diastereomers (*meso* forms). The ^{1}H NMR spectrum of the isolated product pointed to the mixture of diastereomers but all attempts to separate the individual components by HPLC or SFC under various conditions failed. Therefore, the cyclic tetramer **4** has not been studied further in detail.

(Chir)optical and electronic properties of helicene macrocycles 3 and 4

The cyclic trimers homochiral (−)-(*P*,*P*,*P*)-**3** or heterochiral (−)-(*M*,*P*,*P*)-**3** and the cyclic tetramer **4** (a mixture of inseparable stereoisomers) are bright yellow amorphous materials (resins) that exhibit bright blue fluorescence. Their UV-Vis and fluorescence spectra are very similar (Fig. 7). The heterochiral diastereomer (−)-(*M*,*P*,*P*)-**3**, which exemplifies their optical properties, shows a UV-Vis absorption maximum at 349 nm (the onset of the longest wavelength band at *ca.* 450 nm) and an emission maximum in the fluorescence spectrum at 444 nm (the fluorescence quantum yield could not be determined due to the low amounts of resolved stereoisomers). Its optical HOMO–LUMO gap calculated from the UV-Vis or fluorescence spectrum is *ca.* 2.8 eV. Thus, the transition from the parent monomer (+)-(*P*)-**2b** (absorption maximum at 291 nm, absorption onset at *ca.* 426 nm, emission maximum at 429 nm, and an optical HOMO–LUMO gap of *ca.* 2.9 eV) to the cyclic trimer (−)-(*M*,*P*,*P*)-**3** results in only a modest red shift in its optical spectra (about 20 nm). This means that π-conjugation along a large circuit in diastereomeric cyclic trimers/tetramers is somewhat disrupted (π-electron density is partially localised) and, therefore, their optical properties are defined rather by dibenzo[5]helicene subunits. Such behaviour is also reflected in the respective optical (experimentally measured) and calculated HOMO–LUMO gaps (Table 1). It is worth noting that helicene-based macrocycles **3** and **4**, regardless of their stereochemistry, are formally antiaromatic systems (neglecting conformers with

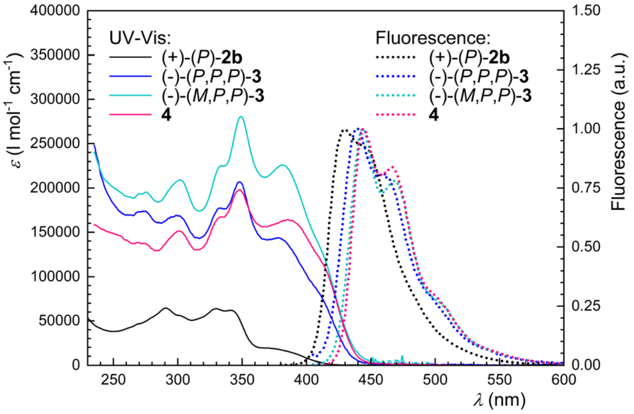

Fig. 7 UV-Vis and fluorescence spectra (in chloroform) of the monomer building block (+)-(*P*)-**2b**, cyclic trimers homochiral (−)-(*P*,*P*,*P*)-**3** and heterochiral (−)-(*M*,*P*,*P*)-**3** and cyclic tetramer **4** (a mixture of inseparable stereoisomers). The intensities of the fluorescence spectra are given in arbitrary units (normalised); excitation wavelengths: 370 nm ((+)-(*P*)-**2b**), 400 nm ((−)-(*P*,*P*,*P*)- and (−)-(*M*,*P*,*P*)-**3**, **4**).

Table 1 Optical and calculated HOMO–LUMO gaps of (+)-(*P*)-**2b**, (−)-(*P*,*P*,*P*)-**3**, (−)-(*M*,*P*,*P*)-**3** and **4** (eV)

Compound	Optical HOMO–LUMO gap[a]	Ground state HOMO–LUMO gap[b]	First excited state HOMO–LUMO gap[c]
(+)-(*P*)-**2b**	2.91 (2.88)	3.56	3.52
(−)-(*P*,*P*,*P*)-**3**	2.79 (2.82)	3.07	3.22
(−)-(*M*,*P*,*P*)-**3**	2.75 (2.79)	3.06	3.21
4[d]	2.75 (2.79)	—	—

[a] Based on the onset of the longest wavelength band in the UV-Vis spectrum or fluorescence maximum (in parentheses). [b] Calculated by DFT (B3LYP/pVDZ/GD3/PCM) in $CHCl_3$. [c] Calculated by TD DFT (CAM-B3LYP/pVDZ/GD3/PCM) in $CHCl_3$, singlet state (E_{SOMO2}–E_{SOMO1}). [d] A mixture of inseparable stereoisomers.

the Möbius topology) as they encompass a 60-electron (cyclic trimer **3**) or an 80-electron (cyclic tetramer **4**) π-conjugated cyclic pathway. These macrocyclic molecules apparently avoid full conjugation (by distorting the structure of the macrocycle and thus lowering the orbital overlap along the macrocyclic circuit) to escape the unfavourable antiaromatic state.

The ECD spectra of the homochiral (−)-(*P*,*P*,*P*)-**3** and heterochiral (−)-(*M*,*P*,*P*)-**3** diastereomers of the cyclic trimer, which were received as individual compounds, are almost identical (Fig. 8). Hence, it is not surprising that the ECD spectrum of the heterochiral (+)-(*M*,*M*,*P*)-**3** and homochiral (+)-(*M*,*M*,*M*)-**3** diastereomers in the inseparable mixture appears as a mirror image of the previous ones. A comparison of the ECD spectra of the laevorotatory cyclic trimers (−)-(*P*,*P*,*P*)-**3** and (−)-(*M*,*P*,*P*)-**3** with the ECD spectrum of the dextrorotatory monomer building block (+)-(*P*)-**2b** shows their very close similarity (the signs of the main bands are the same). Thus, the chiroptical properties of the stereoisomers of the cyclic trimer **3** are mostly determined by the chiroptical properties of the individual dibenzo[5]helicene units, which are partially decoupled from the *trans*-stilbene-4,4′-diyl linkers. It is worth mentioning that the monomer (+)-(*P*)-**2b** and homochiral cyclic trimer (−)-(*P*,*P*,*P*)-**3** encompass the dibenzo[5]helicene unit(s) of the same *P* helicity, but the former is dextrorotatory and the latter is laevorotatory. Although they have markedly similar ECD spectra, *vide supra*, the ECD spectrum of (−)-(*P*,*P*,*P*)-**3** additionally contains a minor band at *ca.* 425 nm, which is negative (the same applies to the heterochiral cyclic trimer (−)-(*M*,*P*,*P*)-**3**). In most cases, the *M* or *P* configuration of helicenes can generally be correlated with the negative or positive sign, respectively, of the longest wavelength ECD band[31] (with a few exceptions[32]). In all cases, the sign of the optical rotation of the helicene macrocycles was derived from the sign of the polarimetric detector signal during chromatographic separation on a chiral column (see ESI, Fig. S7†).

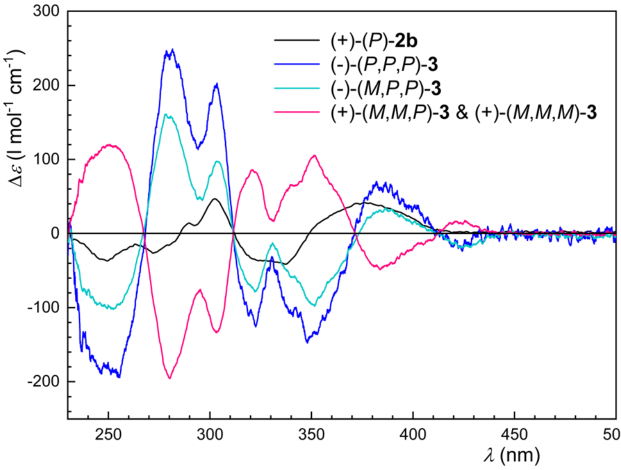

Fig. 8 ECD spectra (in chloroform) of the monomer building block (+)-(*P*)-**2b** and cyclic trimers homochiral (−)-(*P*,*P*,*P*)-**3**, heterochiral (−)-(*M*,*P*,*P*)-**3** and an inseparable mixture of heterochiral (+)-(*M*,*M*,*P*)-**3** and homochiral (+)-(*M*,*M*,*M*)-**3**.

Self-assembly of helicene macrocycles 3 and 4 on a graphite surface investigated by AFM

In our preliminary study, the self-assembly of the helicene macrocycle **3** on a solid surface was addressed with the aim of developing a fast computational method to simulate the formation of molecular stripes and their small-angle symmetry splitting.[18] Imaging helicene macrocycles **3** and **4** by STM on highly oriented pyrolytic graphite (HOPG) encountered the problem of their high mobility on the HOPG surface. The molecules were moved aside by the STM scanning tip, making them essentially invisible in STM unless they were fixed by *e.g.* terrace edges. The use of ambient AFM for high-resolution imaging of molecules represents a notoriously problematic task and not many examples have been published so far.[33–35] Yet when **3** was deposited on HOPG by drop-casting its dichloromethane solution, it was possible to observe ordered molecular self-assemblies well by employing AFM in the PeakForce mode.[36] The precise control of the tip-to-sample interaction enabled by the PeakForce mode, unattainable by other modes, was crucial for successful imaging of the highly mobile macrocycles **3** on the HOPG surface.

Our AFM data clearly show that on the HOPG surface, the highly enantioenriched (>95% ee, dr) homochiral cyclic trimer (−)-(*P*,*P*,*P*)-**3** forms well-ordered domains with a stripe-shaped inner structure (Fig. 9). The orientation of the domains is obviously related to the honeycomb lattice of graphite[37] (defined by unit vectors with an angle of 120°) but it was not possible to resolve the atomic structure of the underlying HOPG surface with high enough resolution to accurately determine the orientation of the domains. Along each main direction, the orientation of the adsorbed molecular domains was found to be split by an angle of 6.5° ± 0.2°. This statistically significant effect is apparently not related to the enantiopurity of the molecules as was also observed in racemic samples. The distance between the centres of adjacent stripes was about 4.80 nm and the length of the stripes could exceed 500 nm. As the diameter of the macrocyclic (−)-(*P*,*P*,*P*)-**3** is about 3.5 nm, the stripes were apparently made up of molecules that self-assembled into tightly packed single rows. With standard contact AFM or recently published higher eigenmode excitation AFM[35] only limited success was achieved. The ordered domains were either destroyed by the scanning AFM tip or the resolution was rapidly lost due to large contamination of the tip by molecules (considerable adhesion force between the tip and the molecules was noticed).

When a mixture of the racemic heterochiral cyclic trimer (*M**,*M**,*P**)-**3** (75%) and racemic homochiral cyclic trimer (*M**,*M**,*M**)-**3** (25%) (*i.e.*, four macrocyclic stereoisomers obtained from the olefin metathesis of *rac*-**2b**) was deposited at low coverage on the HOPG surface, isolated islands were observed consisting of parallel stripes formed by molecules self-assembled into tightly packed single rows (Fig. 10). In the area marked by an arrow, individual macrocycles can be faintly recognised. The figure shows two distinct adsorbate islands with a small splitting (5.4 ± 0.1°) of their surface orientation, which was already observed for enantiopure (−)-(*P*,*P*,*P*)-**3** (*cf.* Fig. 9).[18] It is noteworthy that the adsorbates formed by racemic macrocycles exhibited higher stability during AFM scanning when compared to the assemblies of nonracemic macrocycles leading to submolecular resolution[19] (for details, see the ESI†).

Regardless of the stereochemistry of the cyclic trimer **3**, domains with a stripe-shaped inner structure prevailed when it was drop-cast from solution. The orientation of stripes mostly reflected the hexagonal symmetry of the graphite surface. However, minor stripe-shaped domains with obviously different, more dense packing were also observed in the samples, when the stereoisomers of **3** were scrambled (see the ESI†). In the case of the mixture of the major heterochiral cyclic trimer (−)-(*M*,*P*,*P*)-**3** (75%), its minor enantiomer (+)-(*M*,*M*,*P*)-**3** (17%) and homochiral diastereomer (+)-(*M*,*M*,*M*)-**3** (8%), domains were also found in which the molecules formed long stripes with an unusual width of 6.5 ± 0.1 nm and a separation between 6.3 and 13.3 nm (Fig. 11). Their mutual orientation was nearly orthogonal. Apparently, the molecules in these 1D assemblies formed tightly packed rows that remained largely separated.

The repeated AFM scanning (*ca.* 10×, PeakForce mode) of areas encompassing domains with various ordering and orientation usually resulted in the formation of a large uniform

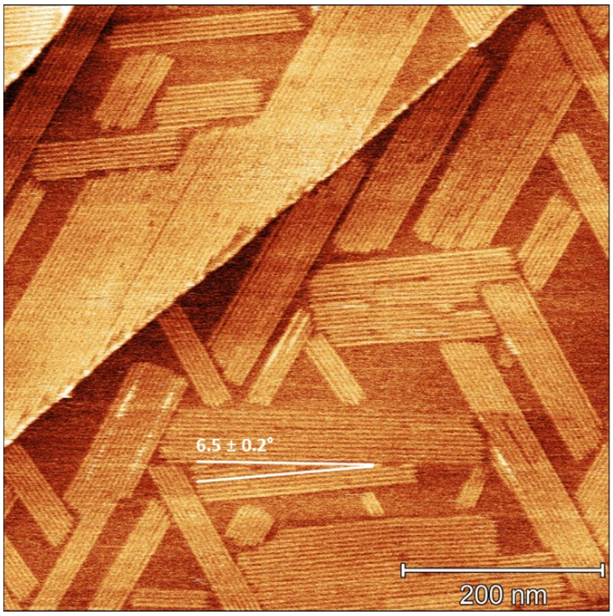

Fig. 9 AFM (PeakForce) image of the self-assembly of a homochiral cyclic trimer (−)-(*P*,*P*,*P*)-**3** (>95% ee, dr on the HOPG surface, Z-scale 800 pm).

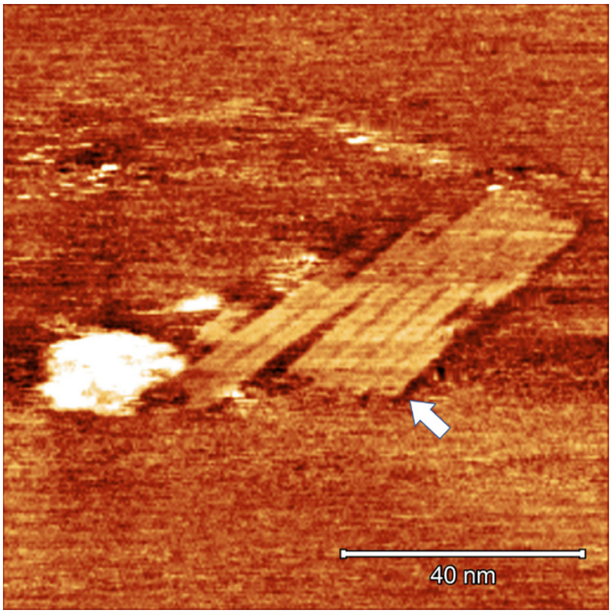

Fig. 10 AFM (PeakForce) image of the self-assembly of the racemic heterochiral cyclic trimer (*M**,*M**,*P**)-**3** (75%) and the racemic homochiral cyclic trimer (*M**,*M**,*M**)-**3** (25%) at low coverage on the HOPG surface. Individual molecules are faintly visible (marked by a white arrow, Z-scale 800 pm); reprinted from *Carbon*[18] with permission from Elsevier.

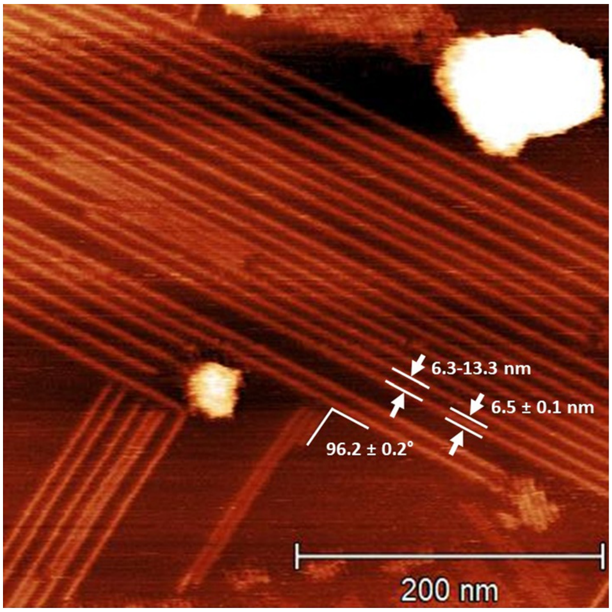

Fig. 11 AFM (PeakForce) image of the self-assembly of the major heterochiral cyclic trimer (−)-(*M*,*P*,*P*)-**3** (75%) in a mixture with its minor enantiomer (+)-(*M*,*M*,*P*)-**3** (17%) and homochiral diastereomer (+)-(*M*,*M*,*M*)-**3** (8%) on the HOPG surface (Z-scale 2 nm).

stripe-shaped domain as a monolayer (for details, see the ESI†). Such mechanically enforced reassembly ("healing") and subsequent uniformity of the 2D molecular crystals indicate that the primary self-assembly of molecules during solvent evaporation is, at least in part, kinetically driven. In samples with higher surface coverage, the molecules self-assembled into crystals several nm tall and up to several microns wide. The molecules from these multilayered crystals could also be redistributed in large stripe-shaped 2D domains by repeated AFM scanning. Interestingly, the step height of 4.8 nm in the crystals was practically identical to the previously observed distance between the centres of adjacent stripes measured in the most abundant stripe-shaped domains. This suggests that the macrocycles in the crystals are arranged with their plane oriented perpendicular to the surface, as opposed to their horizontal arrangement in monolayers (for details, see the ESI†).

Computational simulation of self-assembly of the stereoisomers of macrocycle 3 on the graphite surface

In the AFM images of molecular adsorbates formed by the stereoisomers of the cyclic trimer **3** on the HOPG surface, the motif of long stripes (tightly packed molecules in individual rows, see Fig. 9) was predominant regardless of the stereochemistry of the macrocycles, their combination or surface coverage. Moreover, the macrocycles evidently favoured intermolecular interactions along the rows over interactions between the adjacent rows (stabilising the whole 2D crystal). In order to understand such an intriguing propensity of the stereoisomers of cyclic trimer **3** and to uncover the role of their stereochemistry in self-assembly, molecular dynamics (MD) simulations were employed.

First, attention was paid to the preferred intermolecular orientation studied in five model systems: (i) 18 (*M*,*M*,*P*)-**3** & 18 (*M*,*P*,*P*)-**3** molecules, (ii) 18 (*M*,*M*,*M*)-**3** & 18 (*P*,*P*,*P*)-**3** molecules, (iii) 18 (*M*,*M*,*M*)-**3** & 18 (*M*,*M*,*P*)-**3** molecules, (iv) 18 (*M*,*M*,*M*)-**3** & 18 (*M*,*P*,*P*)-**3** molecules and (v) 36 (*M*,*M*,*M*)-**3** molecules, all placed on the top of a two-layer graphite slab. The stereoisomers of macrocycle **3** were found to be mobile on the surface at the temperature of simulation. This corresponds well to the ease with which molecules move during repeated AFM scanning and the "healing" of monolayers. Following the MD trajectory, molecules soon started to form various gradually growing aggregates until segments of the experimentally observed stripes appeared in the MD simulation (Fig. 12; the final state of the MD trajectory for racemic heterochiral stereoisomers (*M*,*M*,*P*)-**3**/(*M*,*P*,*P*)-**3** is shown).

The most common orientations of macrocycles, which have a triangular scaffold but an outer shape resembling a hexagon due to the presence of six trityl groups, were identified and denoted as edge-to-edge, corner-to-corner and corner-to-edge, all slightly offset (Fig. 13A). Using a custom-made script to statistically analyse the occurrence of these contacts, the final arrangement of macrocycles was found to be dominated by edge-to-edge contacts because they contribute to maximising the attractive van der Waals forces between the interlocked trityl groups. The trityl groups, which are to a certain extent flexible, thus served as a "molecular Velcro" leading to the self-assembly of macrocycles. The time evolution of the contact types between the macrocycles further underlined the

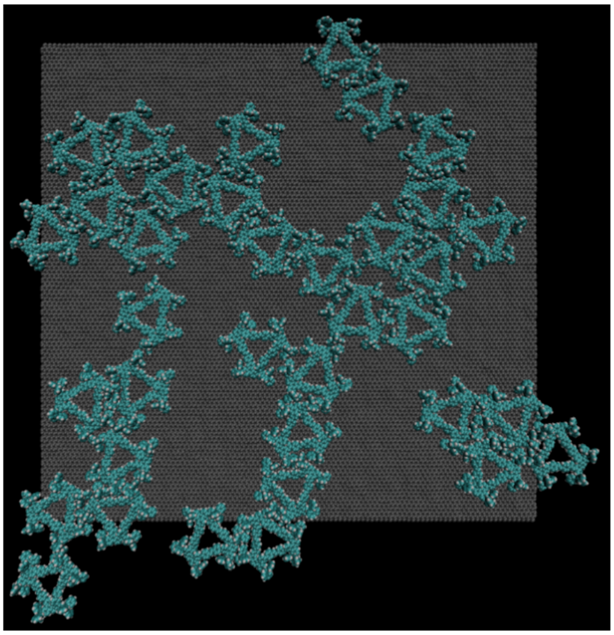

Fig. 12 Final configuration of 18 (*M*,*M*,*P*)-**3** and 18 (*M*,*P*,*P*)-**3** triangular macrocycles obtained from MD simulations (performed as a canonical ensemble at 303 K, 1 fs time step up to 5 ns, integration by the velocity Verlet algorithm, initial velocities were taken from the Maxwell–Boltzmann distribution, using Quantum ATK 2020 software[30,38,39] and ReaxFF force field[40]).

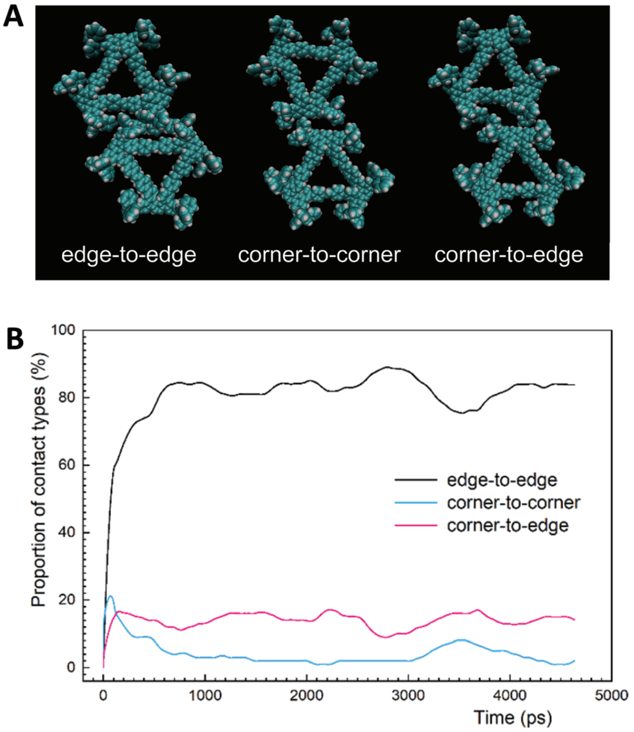

Fig. 13 (A) The most frequent contacts between the stereoisomers of the triangular macrocycle **3**; (B) time evolution of the occurrence of contact types between 18 (*M*,*M*,*P*)-**3** and 18 (*P*,*P*,*M*)-**3** macrocycles during the MD trajectory.

advantage of edge-to-edge contacts, the incidence of which increased rapidly and remained stable during the MD trajectory (Fig. 13B). Similarly, statistical analysis of all the simulated systems mentioned above showed a strong preference for edge-to-edge interaction regardless of the stereochemistry of the macrocycles, which naturally led to a hexagonal-type topology of their aggregates. Nevertheless, the "Velcro" mechanism is likely not the only one governing the self-assembly, and therefore subtle interplay with other effects such as void minimisation, molecule–surface interactions, charge transfer and entropy contribution should also be considered.

To verify the key role of trityl groups in the self-assembly of the aforementioned macrocycles, a system of 36 (*M*,*M*,*M*)-**3*** truncated molecules without trityl groups was subjected to the same MD experiment. Although the molecules had similar surface mobility to their tritylated counterparts, their intermolecular contacts were significantly less stable and larger aggregates did not form. Even gradual cooling after the first 600 ps of the simulation did not help to induce aggregation (at about 60 K, the whole system froze and the molecules remained in their equilibrium positions; for details, see the ESI†). Although the structure of **3** certainly allows for the formation of kinked or cyclic assemblies, only linear aggregates were observed experimentally, even at very low surface coverage. This might reflect the vital role of trityl–trityl and molecule–surface interactions, which are maximized only in densely packed linear aggregates.

Conclusions

To conclude, a helically chiral macrocyclic trimer was synthesised as the major product of a kinetically driven olefin metathesis of a divinyl derivative of tritylated dibenzo[5]helicene. Using racemic or enantiopure starting materials, enantio- and diastereomerically enriched homochiral and heterochiral stereoisomers were obtained. This allowed the description of the energy profile of the interconversion of stereoisomers, which takes place through the inversion of the helicity of the embedded helicene units. The π-conjugation along the large twisted circuit in the helicene cyclic trimer (involving 60 π-electrons) was found to be rather disrupted, stabilising this formally antiaromatic macrocycle. On the HOPG surface, the six-fold tritylated macrocyclic trimers are mobile but self-assemble into long 1D stripes to form stripe-shaped domains, as observed by ambient AFM using the PeakForce mode and corroborated by molecular dynamics simulations. The helicene macrocycles self-assemble regardless of their stereochemistry. The important feature is that the trityl groups not only solubilise helical macrocycles, but also serve as an effective "molecular Velcro" system that stabilises the molecular self-assembly through extensive van der Waals interactions between them (favouring edge-to-edge contacts between the macrocycles while mimicking the well-known function of interdigitated long alkyl chains often employed in 2D-confined molecular self-assemblies). These results significantly expand the very limited knowledge of helically chiral π-electron macrocycles and show that such macrocycles can efficiently self-assemble into well-ordered 2D molecular crystals.

Author contributions

V. H., I. G. S., B. R. and I. S. conceived the project and designed the experiments. V. H. synthesised helical macrocycles. V. H. and J. R. resolved enantiomers/diastereomers by liquid chromatography. V. H. and J. V. performed theoretical calculations and interpreted the results. L. B. measured and interpreted the optical spectra. R. P. measured and interpreted the NMR spectra. V. H. and E. U. performed SPM experiments and interpreted the results. V. H., E. U., I. G. S., B. R. and I. S. analysed and interpreted the data and co-wrote the paper. All the authors discussed the results and commented on the manuscript.

Conflicts of interest

There are no conflicts to declare.

Acknowledgements

This work was supported by the Czech Science Foundation (Reg. No. 20-23566S), the Charles University Grant Agency

(Reg. No. 818319), the European Regional Development Fund (Reg. No. CZ.02.1.01/0.0/0.0/16_019/0000778, CAAS) and the Institute of Organic Chemistry and Biochemistry, Czech Academy of Sciences (RVO: 61388963). We appreciate also the use of CzechNanoLab Research Infrastructure, which was supported by the Ministry of Education, Youth and Sports of the Czech Republic (Reg. No. LM2018110).

References

1 *Helicenes: Synthesis, Properties and Applications*, ed. J. Crassous, I. G. Stará and I. Starý, Wiley-VCH, Weinheim, 2022.
2 B. Thulin and O. Wennerström, *Acta Chem. Scand., Ser. B*, 1976, **30**, 688–690.
3 M. Yamaguchi, H. Okubo and M. Hirama, *Chem. Commun.*, 1996, 1771–1772.
4 H. Okubo, M. Yamaguchi and C. Kabuto, *J. Org. Chem.*, 1998, **63**, 9500–9509.
5 J. M. Fox, D. Lin, Y. Itagaki and T. Fujita, *J. Org. Chem.*, 1998, **63**, 2031–2038.
6 W. Nakanishi, T. Matsuno, J. Ichikawa and H. Isobe, *Angew. Chem., Int. Ed.*, 2011, **50**, 6048–6051.
7 A. Robert, P. Dechambenoit, E. A. Hillard, H. Bock and F. Durola, *Chem. Commun.*, 2017, **53**, 11540–11543.
8 A. Robert, G. Naulet, H. Bock, N. Vanthuyne, M. Jean, M. Giorgi, Y. Carissan, C. Aroulanda, A. Scalabre, E. Pouget, F. Durola and Y. Coquerel, *Chem. – Eur. J.*, 2019, **25**, 14364–14369.
9 A. Ushiyama, S. Hiroto, J. Yuasa, T. Kawai and H. Shinokubo, *Org. Chem. Front.*, 2017, **4**, 664–667.
10 G. R. Kiel, K. L. Bay, A. E. Samkian, N. J. Schuster, J. B. Lin, R. C. Handford, C. Nuckolls, K. N. Houk and T. D. Tilley, *J. Am. Chem. Soc.*, 2020, **142**, 11084–11091.
11 Y. Saiki, H. Sugiura, K. Nakamura, M. Yamaguchi, T. Hoshi and J. Anzai, *J. Am. Chem. Soc.*, 2003, **125**, 9268–9269.
12 G. Naulet, L. Sturm, A. Robert, P. Dechambenoit, F. Röhricht, R. Herges, H. Bock and F. Durola, *Chem. Sci.*, 2018, **9**, 8930–8936.
13 X. Jiang, S. D. Laffoon, D. Chen, S. Pérez-Estrada, A. S. Danis, J. Rodríguez-López, M. A. Garcia-Garibay, J. Zhu and J. S. Moore, *J. Am. Chem. Soc.*, 2020, **142**, 6493–6498.
14 W. Fan, T. Matsuno, Y. Han, X. Wang, Q. Zhou, H. Isobe and J. Wu, *J. Am. Chem. Soc.*, 2021, **143**, 15924–15929.
15 M. Krzeszewski, H. Ito and K. Itami, *J. Am. Chem. Soc.*, 2022, **144**, 862–871.
16 J. Malinčík, S. Gaikwad, J. P. Mora-Fuentes, M.-A. Boillat, A. Prescimone, D. Häussinger, A. G. Campaña and T. Šolomek, *Angew. Chem., Int. Ed.*, 2022, e202208591.
17 F. Feng, T. Miyashita, H. Okubo and M. Yamaguchi, *J. Am. Chem. Soc.*, 1998, **120**, 10166–10170.
18 E. Ukraintsev, V. Houska and B. Rezek, *Carbon*, 2022, **193**, 171–181.
19 E. Ukraintsev, V. Houska, J. Vacek, I. Starý, I. G. Stará and B. Rezek, *Proceedings of the 11th International Conference on Nanomaterials - Research & Application (Nanocon 2019)*, 2020, 561–567.
20 J. Nejedlý, M. Šámal, J. Rybáček, I. Gay Sánchez, V. Houska, T. Warzecha, J. Vacek, L. Sieger, M. Buděšínský, L. Bednárová, P. Fiedler, I. Císařová, I. Starý and I. G. Stará, *J. Org. Chem.*, 2020, **85**, 248–276.
21 A. Jančařík, J. Rybáček, K. Cocq, J. Vacek Chocholoušová, J. Vacek, R. Pohl, L. Bednárová, P. Fiedler, I. Císařová, I. G. Stará and I. Starý, *Angew. Chem., Int. Ed.*, 2013, **52**, 9970–9975.
22 P. Ravat, R. Hinkelmann, D. Steinebrunner, A. Prescimone, I. Bodoky and M. Juríček, *Org. Lett.*, 2017, **19**, 3707–3710.
23 V. Berezhnaia, M. Roy, N. Vanthuyne, M. Villa, J.-V. Naubron, J. Rodriguez, Y. Coquerel and M. Gingras, *J. Am. Chem. Soc.*, 2017, **139**, 18508–18511.
24 K. Traskovskis, I. Mihailovs, A. Tokmakovs, A. Jurgis, V. Kokars and M. Rutkis, *J. Mater. Chem.*, 2012, **22**, 11268–11276.
25 P. E. Romero, W. E. Piers and R. McDonald, *Angew. Chem., Int. Ed.*, 2004, **43**, 6161–6165.
26 *Dynamic Covalent Chemistry: Principles, Reactions, and Applications*, ed. W. Zhang and Y. Jin, John Wiley & Sons, Chichester, 2017.
27 R. H. Janke, G. Haufe, E.-U. Würthwein and J. H. Borkent, *J. Am. Chem. Soc.*, 1996, **118**, 6031–6035.
28 J. Vacek Chocholoušová, J. Vacek, A. Andronova, J. Míšek, O. Songis, M. Šámal, I. G. Stará, M. Meyer, M. Bourdillon, L. Pospíšil and I. Starý, *Chem. – Eur. J.*, 2014, **20**, 877–893.
29 J. Barroso, J. L. Cabellos, S. Pan, F. Murillo, X. Zarate, M. A. Fernandez-Herrera and G. Merino, *Chem. Commun.*, 2018, **54**, 188–191.
30 F. Tavazza, T. P. Senftle, C. Zou, C. A. Becker and A. C. T. van Duin, *J. Phys. Chem. C*, 2015, **119**, 13580–13589.
31 C.-F. Chen and Y. Shen, *Helicene Chemistry: From Synthesis to Applications*, Springer, Heidelberg, 2017.
32 P. E. Reyes-Gutiérrez, M. Jirásek, L. Severa, P. Novotná, D. Koval, P. Sázelová, J. Vávra, A. Meyer, I. Císařová, D. Šaman, R. Pohl, P. Štěpánek, P. Slavíček, B. J. Coe, M. Hájek, V. Kašička, M. Urbanová and F. Teplý, *Chem. Commun.*, 2015, **51**, 1583–1586.
33 D. Klinov and S. Magonov, *Appl. Phys. Lett.*, 2004, **84**, 2697–2699.
34 A. Summerfield, M. Baldoni, D. V. Kondratuk, H. L. Anderson, S. Whitelam, J. P. Garrahan, E. Besley and P. H. Beton, *Nat. Commun.*, 2019, **10**, 2932.
35 V. V. Korolkov, A. Summerfield, A. Murphy, D. B. Amabilino, K. Watanabe, T. Taniguchi and P. H. Beton, *Nat. Commun.*, 2019, **10**, 1537.
36 J. Shi, Y. Hu, S. Hu, J. Ma and C. Su, US8650660B2, 2014.
37 K. Tahara, T. Balandina, S. Furukawa, D. S. Feyter and Y. Tobe, *CrystEngComm*, 2011, **13**, 5551–5558.
38 S. Smidstrup, T. Markussen, P. Vancraeyveld, J. Wellendorff, J. Schneider, T. Gunst, B. Verstichel,

D. Stradi, P. A. Khomyakov, U. G. Vej-Hansen, M.-E. Lee, S. T. Chill, F. Rasmussen, G. Penazzi, F. Corsetti, A. Ojanperä, K. Jensen, M. L. N. Palsgaard, U. Martinez, A. Blom, M. Brandbyge and K. Stokbro, *J. Phys.: Condens. Matter*, 2020, **32**, 015901.

39 J. Schneider, J. Hamaekers, S. T. Chill, S. Smidstrup, J. Bulin, R. Thesen, A. Blom and K. Stokbro, *Model. Simul. Mater. Sci. Eng.*, 2017, **25**, 085007.

40 A. C. T. van Duin, S. Dasgupta, F. Lorant and W. A. Goddard, *J. Phys. Chem. A*, 2001, **105**, 9396–9409.